

# Asymmetrically Substituted Phthalocyanines as Dopant-Free Hole Selective Layers for Reliability in Perovskite Solar Cells

*Peng Huang,<sup>a,†</sup> Adrián Hernández,<sup>b,†</sup> Samrana Kazim,<sup>a,d</sup> Jorge Follana-Berná,<sup>b</sup> Javier Ortiz,<sup>b</sup>*

*Luis Lezama,<sup>c</sup> Ángela Sastre-Santos,<sup>b\*</sup> and Shahzada Ahmad<sup>a,d\*</sup>*

<sup>a</sup>BCMaterials, Basque Center for Materials, Applications and Nanostructures, UPV/EHU

Science Park, 48940 Leioa, Spain,

Tel: +34 946128811 E-mail: shahzada.ahmad@bcmaterials.net

<sup>b</sup>Avda. de la Universidad, s/n, Elche 03202, Spain, E-mail: asastre@umh.es

<sup>c</sup>Departamento de Química Orgánica e Inorgánica, Facultad de Ciencia y Tecnología,

Universidad del País Vasco, UPV/EHU, Sarriena s/n, 48940 Leioa, Spain

<sup>d</sup>IKERBASQUE, Basque Foundation for Science, Bilbao, 48013, Spain

KEYWORDS: perovskite solar cells, metal phthalocyanine, hole transporting materials, improved stability, electron paramagnetic resonance, transient absorbance

## **Abstract**

Dopant-free metal phthalocyanines are viable alternatives to the classical Spiro-OMeTAD in perovskite solar cells (PSCs), due to their appealing optoelectrical properties and chemical stability. However, low carrier concentration, transportability, and narrow bandgap limit their application. Here, we designed and investigated six innovative asymmetrically substituted metal phthalocyanines (MPcs, M = Zn or Cu), and established the correlation between electronic structure, charge carrier transfer parameter, and core metal/substitutions in MPcs by transient absorbance spectroscopy and electronic paramagnetic resonance. We probed the charge transport properties of ZnPcs including carrier lifetime, diffusion coefficient, and diffusion length by transient absorbance spectroscopy. We noted, ZnPcAE presents a longer diffusion length (1.94 nm) than of control ZnPcTB4 (0.80 nm), which is advantageous for reducing charge recombination and gave higher power conversion efficiency in the fabricated PSCs. Importantly, the devices with MPcs yielded improved stability under multi-stress conditions. Our work provides a molecular guideline for designing MPcs and their application as dopant-free hole-transporting materials for perovskite solar cells fabrication.

## **1. Introduction**

Hybrid organic-inorganic perovskite solar cells (PSCs) have attracted significant interest, as their certified power conversion efficiency (PCE) swiftly soared from 10% to 25.5% in less than a decade.<sup>1-3</sup> This rapid advancement in the figure of merit was due to the unparalleled characteristics of hybrid organic-inorganic perovskites: tuneable panchromatic light absorption, long carrier diffusion lengths for electrons/holes, and low-temperature solution-processability.<sup>4-6</sup> To accelerate the commercial viability of perovskite-based devices, the investigation on the stability of

perovskite and the device is receiving substantial attention. Designing innovative electron/hole-transporting materials (ETM/HTM),<sup>7,8</sup> placement of a buffer layer at the different interfaces<sup>9</sup> allowed to optimize the photovoltaic (PV) performance and device stability.<sup>10,11</sup>

In typical (*n-i-p*) PSCs, the HTMs coated perovskite layers play crucial roles in separating and extracting photo-generated holes, suppressing interface charge recombination, to achieve high PCE. The choice of HTMs can extend the durability of the devices by isolating the perovskite active layer from oxygen, moisture, and passivating the surface defect. Although 2,2',7,7'-tetrakis-(*N,N*-di-*p*-methoxyphenylamine)-9,9'-spirobifluorene (Spiro-OMeTAD), is the most employed HTM in *n-i-p* type PSCs, the pristine Spiro-OMeTAD possesses poor electrical properties, UV instability, and is cost-ineffective.<sup>12,13</sup> Further the use of hygroscopic *p*-type dopants and additives such as lithium bis(trifluoromethanesulfonyl)imide (Li-TFSI) and 4-*tert*-butylpyridine (*t*-BP), or metal complex is a prerequisite to improve electrical properties, which diffuses into perovskite layers and accelerate degradation under real operating conditions.<sup>12,13</sup> Alternatively, developing dopant-free HTMs that can yield high PV performance and stability is paramount research.

Recently, the dopant-free HTMs based on small molecules, macrocycle molecules, and conjugated polymers, have been designed and their performance was reported.<sup>14</sup> Phthalocyanines (Pcs) are attractive as HTMs due to their ease of synthesis, purification steps and are thermally and photochemical stable. In most of the cases, they yield competitive performance in PSC,<sup>15</sup> except the report of symmetrical NiPc with four methoxy-ethoxy measured over 21% efficiency.<sup>16</sup>

The PV performance of the PSCs employing Pcs is limited by two major factors: (i) poor conductivities of pristine Pcs. In the early stages of Pcs based HTMs development, dopants (lithium salts and *t*-BP) were inevitable to introduce for improvement of transporting ability, which sacrifices the device stability.<sup>17</sup> Aiming for developing dopant-free Pc HTMs, various peripheral /

non-peripheral substituents, and different core atoms were applied into phthalocyanine.<sup>18</sup> Non-peripheral *P*-SC<sub>6</sub>-TiOPc / peripheral-substituted *NP*-SC<sub>6</sub>-TiOPc dopant-free HTMs were synthesized.<sup>19</sup> We have designed peripheral-substituted ZnTTPc with tetra-thienyl-methoxytriphenylamine (TTPA),<sup>20</sup> while report of different tetra-methoxy-ethoxy-based Pcs with diverse core atoms (H<sub>2</sub>, Zn, Cu, Ni, and Co) also appears.<sup>16</sup>

(ii) Interface recombination triggered their narrow bandgap ranging from 1.4 eV – 2.1 eV. The phenomena induced poor electron blocking and charge recombination at the perovskite/HTM interface. Although the introduction of substituents or the interplay of central atoms can tune the bandgap of Pcs and alleviate the interface recombination, the limited opportunity of bandgap tuning is not effective. Improving the carrier diffusion length ( $L_D$ ) of the Pcs, which was determined by the exciton or carrier lifetime ( $\tau_E$ ) and diffusion coefficient ( $D_E$ ), as well as the carrier mobility ( $\mu$ ) is an effective protocol to impede the interfacial charge recombination. In this context, heavy palladium as core atom to replace copper atom in Pcs with octamethyl substituents was investigated and it was noted that PdPc presented longer  $L_D$ , and thus delivered a higher performance.

Until now, the correlation between electronic structure, charge carrier transfer parameters (lifetime, diffusion coefficient, diffusion length), and the core metal and substitutions in MPcs are not well deciphered. Herein, we elaborately designed a series of peripheral substituents including 2-methoxyethan-1-amine (AE), thiadiazole (TDZ), and TTPA to induce asymmetry in terms of the symmetrical MPc with four tert-butyl groups (M= Zn or Cu, **Figure 1**). Notably, asymmetrical substituted-phthalocyanines owned unique photophysical and electrochemical properties as compared to symmetrical Pcs, stems from the perturbing the distribution of the 18- $\pi$ -delocalized electrons over the macrocycle. We unravel the Pcs properties are controlled by core metal and

substitutions, through transient absorbance, electron paramagnetic resonance, respectively. Further, to probe the practical utility, we fabricated PSCs by employing MPcs as dopant-free HTM (Figure 1). Arguably, the fabricated devices gave excellent stability under multi-stress conditions (moisture, heating, and light).

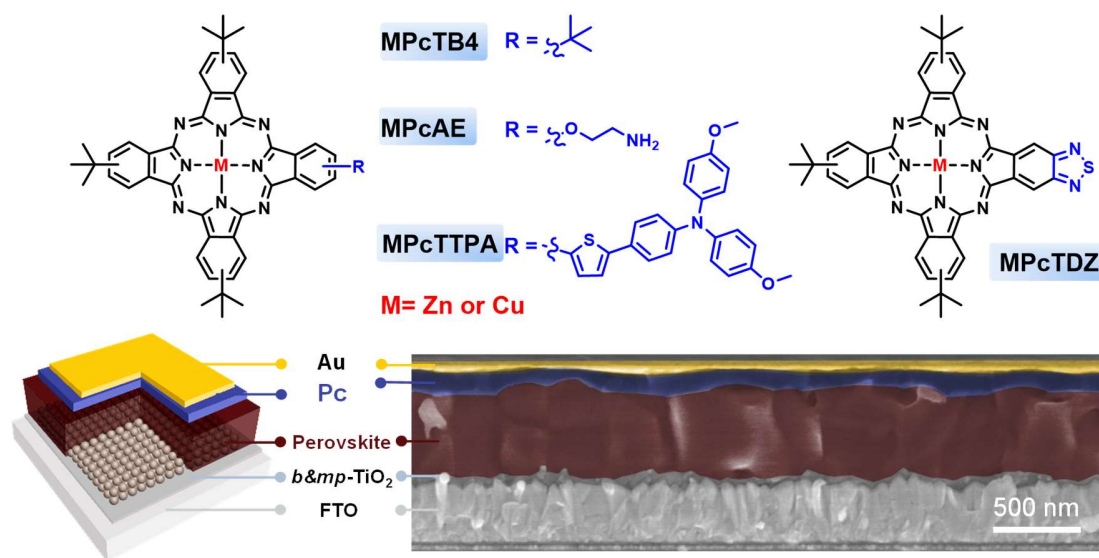


Figure 1. the molecular structures of unsymmetrical MPcs and device architect employing MPc as an HTM, and the representative cross-sectional image of PSC with standard architecture FTO/*b&mp*-TiO<sub>2</sub>/perovskite/ZnPcAE/Au.

## 2. Results and discussion

### 2.1 Synthesis

Synthesis of ZnPcTB<sub>4</sub>, ZnPcTDZ and ZnPcAE were carried out following the procedures for ZnPcTB<sub>4</sub>,<sup>21</sup> ZnPcTDZ,<sup>22</sup> and ZnPcAE.<sup>23</sup> Firstly, we describe the synthesis of CuPcTB<sub>4</sub> and CuPcTDZ (Figure S1a). Due to the difficulty in the purification of CuPcTB<sub>4</sub> and CuPcTDZ obtained from statistical cyclotetramerization of respectively phthalonitriles in the presence of Cu(OAc)<sub>2</sub>, it was essential to synthesize the free-base phthalocyanines from the corresponding

diiminoisoindolines. H<sub>2</sub>PcTB4 and H<sub>2</sub>PcTDZ, were obtained by reaction of diiminoisoindoline 1<sup>24</sup> and diiminoisoindoline 2 and subsequent isolation by chromatographic column with 13% and 9% yield, respectively. Then, metallation using Cu(OAc)<sub>2</sub> allowed to obtain CuPcTB4 and CuPcTDZ with 76% and 79% yield, respectively. Second, we prepared CuPcAEBoc (Figure S1b) by statistical cyclotetramerization of phthalonitrile 3 and phthalonitrile 4 with CuCl<sub>2</sub>. After a careful purification by chromatography column (Et<sub>3</sub>N-deactivated SiO<sub>2</sub>) the product was obtained with a 5% yield. We removed the 2-*tert*-butoxycarbonyl group in acid conditions yielding CuPcAE in 88% yield.

Third, synthesis of ZnPcTTPA (Figure S1c) was performed by statistical cyclotetramerization of *tert*-butyl-phthalonitrile 3 and thienyl-methoxytriphenylamine- phthalonitrile 5,<sup>20</sup> in the presence of Zn(OAc)<sub>2</sub>. After purification by column chromatography ZnPcTTPA was obtained (18% yield). The <sup>1</sup>H-NMR spectra of ZnPcTTPA in THF-*d*<sub>8</sub> showed well-defined aromatic and aliphatic signals (Figure S16). The three isoindole units with the *tert*-butyl groups show different signals in the aromatic zone at 9.55, 9.39, and 8.32 ppm. Instead, the isoindole with the aromatic chain shows three signals at 9.39, 8.45, and 7.95 ppm. Regarding the aromatic chain, two doublets from the thiophene (9.67 and 7.50 ppm), four doublets from the phenyl group (7.91, 7.65, 7.12, and 7.00 ppm), and a singlet from the methoxy groups (3.80 ppm) are shown. Finally, for the synthesis of CuPcTTPA (Figure S1c) a similar procedure was followed, using CuCl<sub>2</sub> instead of Zn(OAc)<sub>2</sub>. Subsequently, purification was made by column chromatography (Et<sub>3</sub>N-deactivated SiO<sub>2</sub>), CuPcTTPA was obtained (12% yield). Due to the paramagnetic character of copper (II), characterization by NMR experiments was not possible for any CuPcs. Nevertheless, they were characterized by FT-IR, HR-MALDI-TOF, and UV-Vis experiments, respectively. (Figure S2–S22).

## 2.2 Electro-optical and physical properties

The normalized absorption spectra of MPcs in solvents and solid films (Figure 2a & 2b), are displayed and the stronger peak at the Q band was used as the standard for normalization. The Soret bands (B bands) are located in the ultraviolet region (300–430 nm), which is linked to the transitions from  $S_0$  to  $S_2$  (ground state to second excited state). We attribute the appearance of a trivial shoulder at ~615 nm to the vibronic band. Strong absorption (600 – 800 nm) suggests the Q band signal and is related to the transition from  $S_0$  to  $S_1$  (ground state to first excited state), and interpreted as  $\pi$ - $\pi^*$  excitation between bonding and antibonding molecular orbitals.

For the absorption spectra of the MPc in solvents, the Q band of MPcAE in the solvent is similar to MPcTB4 (Figure 2a), while the Q band of MPcTDZ and MPcTTPA split into doublet Q bands, which is attributed to the presence of different regioisomers and also by the breaking of the  $D_{4h}$  symmetry.<sup>25</sup> Besides, the Q band of MPcTDZ displays the widest absorbance from 500 – 785 nm and showing another band situated at 723 nm for ZnPcTDZ and 736 nm for CuPcTDZ, respectively because of the thiadiazole ring. The absorption spectra of MPcTTPA is bathochromically shifted compared to that of MPcTB4 and exhibited broadened absorption in contrast to that of MPcTB4.

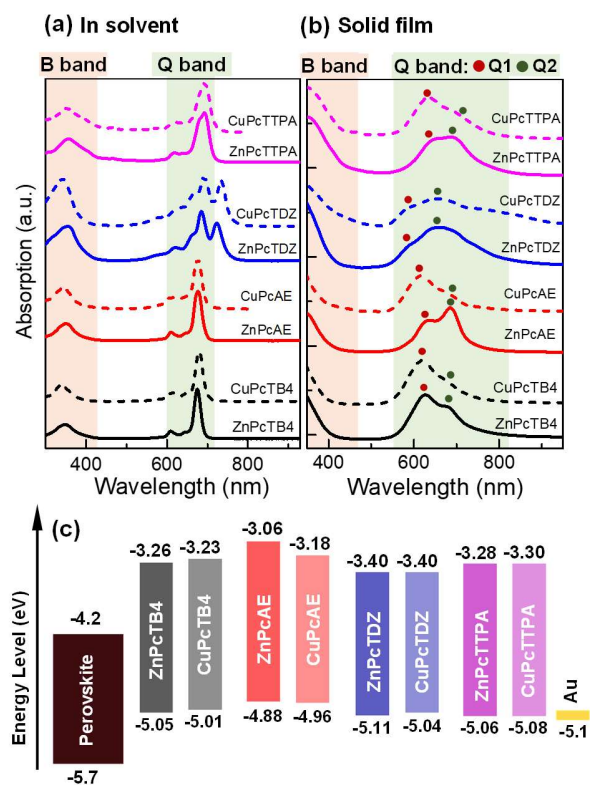


Figure 2. UV-vis absorption spectra of MPcs in (a) solution and (b) solid films, and (c) energy level diagram for the hole transporting side for all the MPcs.

The absorption spectra of the films on quartz (Figure 2b) display a spread of the signals from red and blue by comparing with the solution spectra (Figure 2a), the absorption of MPc films displays wide Q bands from 550 – 800 nm. When compared with the MPcTB4, a slight bathochromic shift is observed in MPc with other substitutions. This phenomenon can be related to the formation of aggregates, which can affect the charge carrier transport in the solid film.<sup>26,27</sup>

The peak absorption band at short wavelength named Q1 is contributed to aggregated species, and face-to-face stacking of the molecules, while the other peak absorption at long wavelength called Q2 is attributed to the monomeric species.<sup>28</sup> The primary species of MPcs were evaluated



from the relative intensities of Q1 and Q2 bands. For ZnPcs, the ZnPcTB4 holds the main aggregated species, but other ZnPcs owned the main monomeric species. It illustrates that different substitutions can control the aggregation in the film and charge carrier transport. However, apart from CuPcTDZ with monomeric species, the other CuPcs show rich aggregated species.<sup>28,29</sup>

The asymmetrical MPcs with TDZ and TTPA substituents displayed distinct absorption in the solution while MPcs with AE group display similar absorption curves as of reference (MPcTB4). Arguably, the optical properties of the new MPcs could be controlled by the asymmetrical substitution groups. Importantly, the primary species of MPcs in the solid films for asymmetrical ZnPcs is monomeric species, while in ZnPcTB4 is aggregated ones. In contrast, the trend of primary species in CuPcs is not in a similar fashion as ZnPcs, suggesting the primary species can be tuned by the asymmetrical group and core metal synergistically.

To evaluate the energy level alignment of the perovskite/MPcs interface, we performed electrochemical characterization using differential pulse voltammetry (Figure S23-S27 in the supporting information) and ferrocene redox couple as the external standard (Table S1 in the supporting information). The highest occupied molecular orbital energy levels ( $E_{\text{HOMO}}$ ) deduce from the Equation:  $E_{\text{HOMO}} = -4.8 - E_{\text{ox}}$ , where  $E_{\text{ox}}$  is the first onset oxidation potential. The lowest unoccupied molecular orbital energy levels ( $E_{\text{LUMO}}$ ) of MPcs were determined by adding the optical bandgap to  $E_{\text{HOMO}}$  value. The schematic diagram displays the energy level of PSCs (Figure 2c) and the energy levels of reported MPcs (ZnPcTB4, ZnPcAE, and ZnPcTDZ) noted from the literature. We noted that asymmetrical MPc with a similar substitution but with different core metals presents similar  $E_{\text{HOMO}}$  and  $E_{\text{LUMO}}$ , while different substitutions influence the semiconducting properties. The energy levels of the asymmetrically MPc with TDZ, TTPA show a trivial difference, but asymmetrical MPcAE have slightly higher than reference, may be ascribed

to the ammonia as end arms. Assuming the valence band/conduction band of mixed-ion perovskite are at -5.7 eV/-4.2 eV, all the  $E_{\text{HOMO}}$  of MPcs are energetically favorable, signaling an efficient charge extraction at the interfaces. The  $E_{\text{HOMO}}$  of MPcTDZ is lying lowest than that of other MPcs, thus a higher open-circuit voltage ( $V_{\text{oc}}$ ) of the corresponding device can be expected. Owing to the narrow bandgap of MPcs, the highest value is 1.82 eV for ZnPcAE, and the lowest value is 1.64 eV for CuPcTDZ. Arguably, the photo-generated electron will be also transported by MPcs and increase the interface recombination, while ZnPcAE with higher  $E_{\text{LUMO}}$  is potentially attractive to block the electron effectively as compared to others.<sup>30</sup>

### 2.3 Ultrafast Transient Absorbance Studies

To unravel the carrier transport properties in these asymmetrical MPcs and probe its correlation with core metal and substitution, we investigated the charge carrier dynamics of thin films via transient absorption spectroscopy (TAS). The TAS spectra (Figure 3a) in the visible range at the indicated delay times, presented a broad positive signal (peak) at the wavelength region between the B band and Q band, which is typically associated with the singlet and triplet excited-state absorption of photo-generated carrier or excitons in the film.<sup>31,32</sup> The broad negative signals (trough) at the wavelength region of the Q band was characterized to the overlapping between the ground-state bleaching (GSB) and the stimulated emission (SE) for Soret fluorescence, where the GSB is stemmed from the depletion of the population in the ground electronic state following photoexcitation. We noted the profile of TAS mismatch with the static absorption (Figure S28). All the ZnPc samples display a faster decaying on a picosecond timescale (10 ps) and near-complete decay reaching nanoseconds. However, the CuPcs presents dissimilar decay phenomena except for CuPcAE, compared to Zn-based counterparts, CuPcTB4 showed a signal increase

within hundreds of picoseconds, but CuPcTDZ and CuPcTTPA presented no decay within this time frame (hundred of picoseconds). The signal of all CuPcs showed only half decay value reaching nanoseconds.

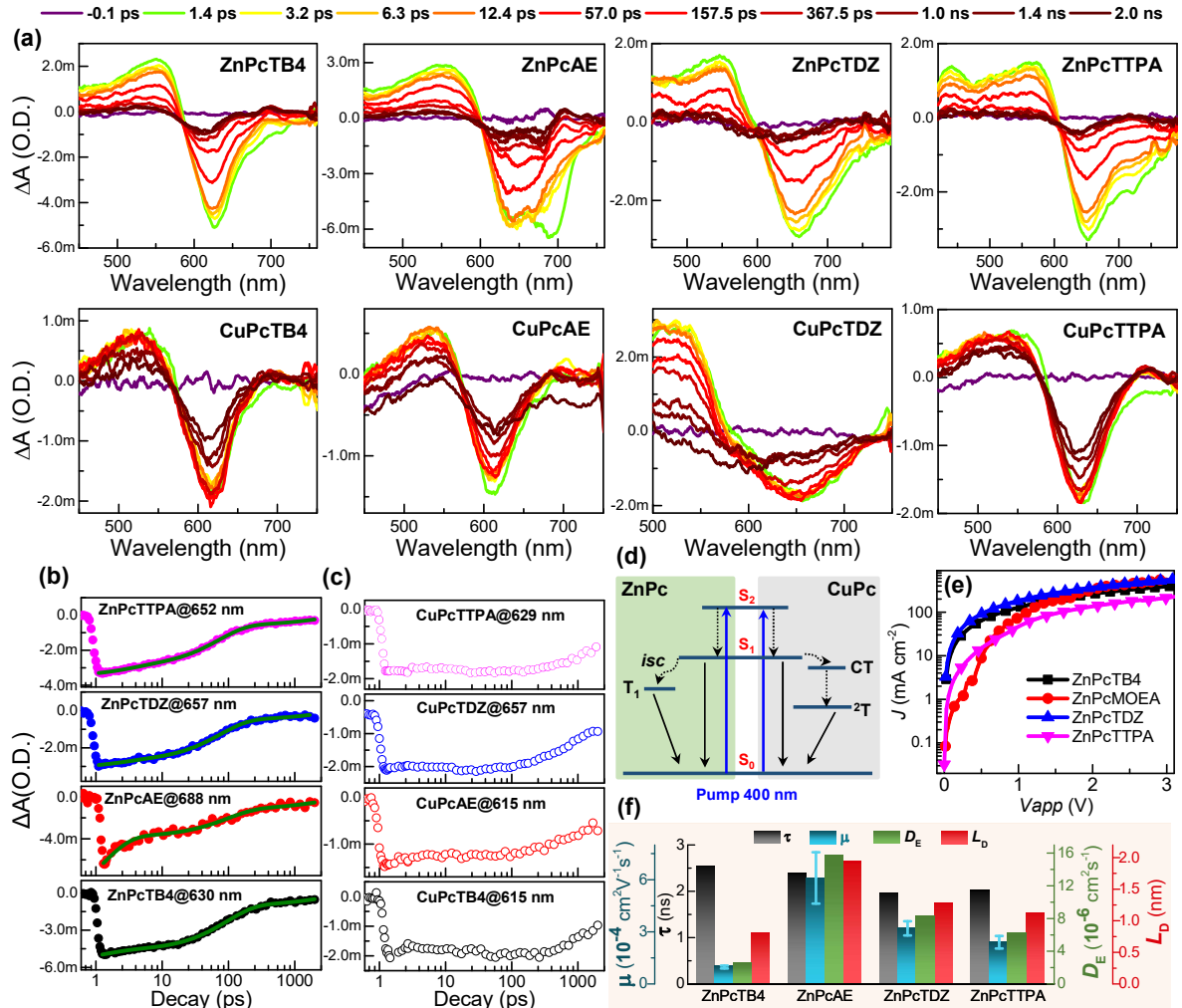


Figure 3. (a) TA spectra evolution of ZnPcs and CuPcs at indicated times (details in the legend). All the samples were spin-coated on a quartz substrate. Kinetic traces of (b) ZnPcs and (c) CuPcs at maxima GSB signal point, (d) schematic diagram of the energy relaxation dynamics of the ZnPc and CuPc, (e)  $J$ - $V$  curves of the ZnPcs based hole-only device with the structure: FTO/PEDOT:PSS/HTM/Ag and (f) summary of the charge transfer parameters of ZnPcs.

We investigated the dynamic traces of ZnPcs and CuPcs at the trough point (Figure 3b&3c) to clarify the charge kinetic decay process. The three timescales can be distinguishably observed for ZnPcs: the first fast decay within the first few picoseconds can be ascribed to the intersystem crossing (*isc*) from ( $S_1 \rightarrow T_1$ ) because the internal conversion ( $S_2 \rightarrow S_1$ ) occurs within femtoseconds timescale. The other two components correspond with the repopulation of the ground state ( $S_0$ ) including two branches: a substantial decay from exciton state via exciton-phonon coupling ( $S_1 \rightarrow S_0$ ) with hundred picoseconds and slow decay with nanoseconds via non-radiative relaxation of the triplet state ( $T_1 \rightarrow S_0$ ). We draw a schematic diagram for MPcs illustrating the entire transient process (Figure 3d).

The traces of ZnPcs were well fitted with a tri-exponential function with the decay equation:  $I(t) = \sum \alpha_i \exp(-t/\tau_i)$ , where  $I(t)$  is the total transient absorption decay curve, and  $\alpha_i$  and  $\tau_i$  are relative amplitude and lifetime of the  $i$ th component (the normalization condition being  $\sum \alpha_i = 1$ ), respectively (Table S2). The range of carrier lifetime is in agreement with the reported values.<sup>33,34</sup> The carrier lifetime for asymmetrical ZnPcs with different substitutes is similar with reference (ZnPcTB4). However, ZnPcAE have the larger amplitude value (0.65) than ZnPcTB4 (0.21), ZnPcTDZ (0.12), and ZnPcTTPA (0.16). We attribute this discrepancy in lifetime and amplitude to the stronger spin-orbit coupling effect introduced by substitution groups in asymmetrical ZnPcs.

All the CuPcs showed longer relaxation kinetics than the Zn-based counterparts. The CuPcTB4 and CuPcMOEA samples showed faster relaxation within the first 2 picoseconds. The Cu element (atomic number 29) has an unfilled d-orbital with an electronic configuration of  $3d^9 4s^2$  in contrary to Zn element (atomic number 30) owned a fill d-orbital with an electronic configuration of

$3d^{10}4s^2$ , indicating that Cu-based Pcs achieve a higher probability of donor-acceptor interaction between core Cu metal and peripheral groups.

The CuPc derivatives can be populated by relaxing its excited singdoublet state ( $^2S$ ) through the ligand-to-metal charge transfer (CT) to a triplet (tripdoublet) state of  $^2T$  with a sequential decay passage of  $^2S_1 \rightarrow ^2CT \rightarrow ^2T$ .<sup>25,31,35</sup> Because the decay process in CuPcs does not accept a direct flip of the electronic spin state,<sup>31,36,37</sup> which was evidenced to be more swift and efficacious than the decay process in ZnPcs, in which  $i_{sc}$  transition is accountable for the  $S_1 \rightarrow T_1$  decay. Similar phenomena were reported in copper-based porphyrins and phthalocyanines.<sup>31,37,38</sup> Faster decay curves for CuPcTDZ and CuPcTTPA were not observed by us within the first 2 ps can be explained mainly by the fast decay via CT and stimulated emission.

Unlike the signal of corresponding ZnPcs at maxima point showing a continuous decay, the CuPc(TB4, TDZ, TTPA) shows no significant change in decay within the hundred picoseconds, and CuPcAE have slower decay than ZnPcAE. As referred above, the trough signal was controlled by GSB and SE, the absent decay or slower decay of CuPcs resulted from the stimulated emission. It indicates that stimulated emission in CuPcs can increase the decay lifetime because of the unique electronic structure of Cu elements.<sup>39,40</sup> The decay curves divergence of all CuPcs ascribed to that different substitution, which can affect the triplet process, and probably originated from the improved molecular interaction and increase of the Forster energy transfer process, which lead to excitation coupling with  $\pi \rightarrow \pi^*$  transitions between closed molecules.

For phthalocyanine, the energy relaxation process should make the signal eventually decay to zero at a more extended time decay. The strong GSB of CuPcs finally evolves into a long-lived process and does not finish their decay in our detection window (2.0 ns). We ascribed the longer lifetime in CuPcs to the strong spin-orbit coupling effect introduced by the Cu atom. The

stimulated emission phenomena in CuPc are stronger than the corresponding ZnPcs, which can increase the lifetime of CuPcs.

In all, the core metals and different substitutions of the asymmetrical MPcs, the charge decay process is synergistically controlled in the solid film. The asymmetrical MPcs have no measurable influence on the lifetime of the decay process, their impact on the amplitude for intersystem crossing by inhibiting molecular aggregation, playing role in donor/acceptor. Compared to Zn as core metal, the Cu element with unfilled d-orbitals own unique decay process ( $^2S_1 \rightarrow ^2CT \rightarrow ^2T$ ) and increase decay via stimulated emission, and has a longer lifetime. The asymmetrical MPcs and core metals can affect the triplet state properties that in turn influence the transportation of electrons and holes.

At first instance, the longer  $\tau_e$  of MPcs of triplet state excitons emerge to show viability for increasing diffusion length ( $L_D$ ) via the triplet sensitization pathway. On the contrary, the longer  $\tau_e$  are offset for the significantly reduced diffusion coefficient ( $D_E$ ), Because the Forster resonance energy transfer for (pure) triplet state diffusion is spin-forbidden, while a Dexter energy transfer with a much shorter operating range will essentially take charge of the energy migration process.<sup>41</sup>

The hole mobility ( $\mu$ ) of ZnPcs were determined by space-charge-limited current measurement (Figure 3e), and the corresponding  $D_E$  was derived according to the Einstein relation with a classical equation:  $D_E/\mu = kT/q$ , where  $k$  is the Boltzmann coefficient,  $q$  is the charge of electron or hole, and  $T$  is the measuring temperature. The average value of hole mobilities for ZnPcs follows the order: ZnPcAE ( $\sim 6.10 \times 10^{-4} \text{ cm}^2 \text{ V}^{-1} \text{ s}^{-1}$ ) > ZnPcTDZ ( $\sim 3.21 \times 10^{-4} \text{ cm}^2 \text{ V}^{-1} \text{ s}^{-1}$ ) > ZnPcTTPA ( $\sim 2.4 \times 10^{-4} \text{ cm}^2 \text{ V}^{-1} \text{ s}^{-1}$ ) > ZnPcTB4 ( $\sim 0.97 \times 10^{-4} \text{ cm}^2 \text{ V}^{-1} \text{ s}^{-1}$ ). The corresponding  $D_E$  of ZnPcs was calculated (Figure 3f and Table 1) and follows the order ZnPcAE ( $15.81 \times 10^{-6} \text{ cm}^2 \text{ s}^{-1}$ ) > ZnPcTDZ ( $\sim 8.32 \times 10^{-6} \text{ cm}^2 \text{ s}^{-1}$ ) > ZnPcTTPA ( $6.22 \times 10^{-6} \text{ cm}^2 \text{ s}^{-1}$ ) > ZnPcTB4 ( $2.52 \times 10^{-6} \text{ cm}^2$

s<sup>-1</sup>). Although the Forster resonance energy transfer for pure triplet state diffusion is spin-forbidden, the highest amplitude of ZnPcAE for  $i_{sc}$  process showing a substantial singlet character in its T<sub>1</sub> state, and enhanced spin-orbit coupling. It is sufficient to enable Forster resonance energy transfer to appear. This singlet-triplet mixing could increase the  $\mu$  and  $D_E$ , and then  $L_D$ . The  $L_D$  of ZnPcs was thus calculated according to the equation  $L_D = (D_E\tau_E)^{1/2}$ , and the relevant parameters are summarized (Table 1). The  $L_D$  of ZnPcs showed the following order: ZnPcAE (1.94 nm) > ZnPcTDZ (1.28 nm) > ZnPcTTPA (1.12 nm) > ZnPcTB4 (0.80 nm). Longer  $L_D$  can improve charge transportability via inhibiting the carrier recombination induced by their narrow bandgap in the transporting layer and thus boost the higher efficiency.

Table 1 Summary of the charge transfer parameters of MPcs.

HTM	$\tau_{ave}$ (ps)	$\mu$ ( $10^{-4}$ cm <sup>2</sup> V <sup>-1</sup> s <sup>-1</sup> )	$D_E$ ( $10^{-6}$ cm <sup>2</sup> s <sup>-1</sup> )	$L_D$ (nm)
ZnPcTB4	2535.7	0.97	2.52	0.80
ZnPcAE	2380.0	6.10	15.81	1.94
ZnPcTDZ	1963.2	3.21	8.32	1.28
ZnPcTTPA	2005.1	2.40	6.22	1.12

To establish the variation in electrical properties of ZnPcs with different substitutions, molecular orientation, and microstructure of MPcs was investigated. The grazing incidence X-ray diffraction (GIXRD) pattern was measured on FTO and perovskite coated Pc substrates (Figure S29 in the supporting information). The ZnPcs with substitutions showed no peak in the GIXRD patterns, indicating the amorphous nature. We investigated the film-forming ability of ZnPcs with the aid of scanning electron microscopy (SEM) and atomic force microscopy (AFM) (Figure S30)

techniques. The uniform and fine coverage of perovskite layers with symmetrical ZnPc suggest its film-forming ability.

## 2.4 Electron paramagnetic resonance

To probe the possible interaction and relationship between the electronic structure of the phthalocyanine metal center and its photovoltaic performance, we recorded the electron paramagnetic resonance (EPR) spectra of the isostructural copper compounds.

The X-band room temperature EPR spectra of CuPcTB4, CuPcAE, CuPcTDZ, and CuPcTTPA solid samples show quasi-isotropic signals, centered about  $g=2.07$ . We noted that neither the shape nor the position of the signal showed any noticeable changes, a clear variation of the peak-to-peak line width was observed in the order: CuPcTB4 < CuPcTDZ < CuPcAE < CuPcTTPA. The Q-band spectra are better resolved showing the axial  $g$  anisotropy characteristic of copper (II) phthalocyanine complexes (Figure 4a & 4b).<sup>42-46</sup> The  $g$  values are obtained by simulation of the experimental spectra (Table S3). In all the cases, the lowest  $g$  deviates significantly from the free-electron value ( $g_e=2.0023$ ) and  $g_{\parallel}$  is higher than  $g_{\perp}$ , thus the unpaired electron is occupying the  $d_{x^2-y^2}$  orbital in the equatorial plane of a Cu (II) chromophore with elongated tetragonal symmetry. The calculated  $g$  values are in agreement with those observed in other CuPc complexes.<sup>44,45</sup> The absence of resolved copper and nitrogen hyperfine structure is due to dipolar and/or exchange interactions between Cu (II) ions from different molecules.

To elucidate if the  $g$  values obtained from the solid-state experiments are molecular, we also investigated using the  $G$  parameter proposed by Hathaway [ $G=(g_{\parallel}-2)/(g_{\perp}-2)$ ] which lies in the 4.4–4.9 range when the  $g$  values are equal to molecular values.<sup>47</sup> In this case,  $G$  is close to 3 for all the compounds, which implies that the  $g$  values are averaged due to spin-spin interactions. In



this context, the smaller peak-to-peak linewidth observed in the EPR spectra of CuPcTB4 implies that the exchange interactions in this solid are more efficient than in the other complexes.

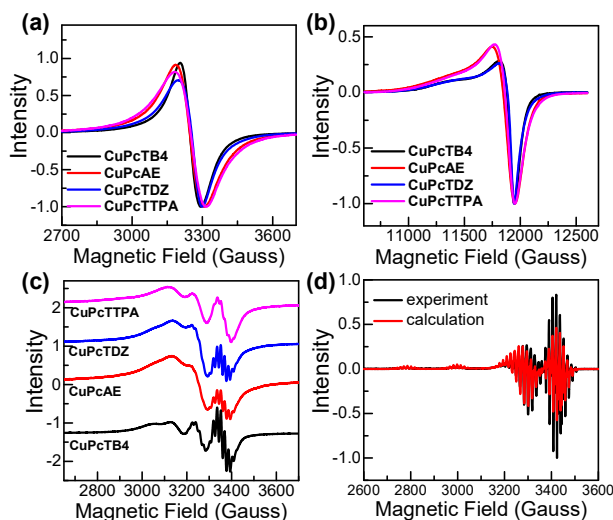


Figure 4. (a) X-band and (b) Q-band EPR spectra of CuPc solid samples at room temperature, (c) X-band room temperature EPR spectra of CuPc complexes dissolved in toluene, and (d) experimental and simulated EPR spectra of CuPcTB4 in toluene at 100 K.

To reduce the spin-spin interactions, to improve the resolution of the EPR signal, and to derive further information over the effects of the substitution of peripheral ligands on the electronic structure and bonding, the copper complexes were dissolved in toluene. In all the cases, the X-band solution of EPR spectra recorded at room temperature (Figure 4c) show four hyperfine lines due to the interaction of Cu(II) unpaired electron with the copper nuclei ( $I = 3/2$ , isotopes  $^{63}\text{Cu}$  and  $^{65}\text{Cu}$ ). Besides, a super hyperfine splitting due to the presence of four geometrically equivalent  $^{14}\text{N}$  nuclei ( $I = 1$ ) can be observed. Moreover, the line widths show the typical dependence with the nuclear quantum number  $M_I$  ( $\Gamma = \alpha + \beta M_I + \gamma M_I^2$ )<sup>48</sup> due to molecular tumbling effects, with better resolution on the  $M_I = +1/2$  and  $+3/2$  lines, especially for the CuPcTB4 compound. Considering that the concentration of spins was similar in all solutions, the main causes of the

different resolutions observed for each compound must be the molecular tumbling. The tumbling coefficients depend on the anisotropies of  $g$  and of the hyperfine couplings and on the rotational rate<sup>44</sup>. By simulation of the room temperature solution spectra (Figure S31) the isotopic values of  $g$ ,  $A_{\text{Cu}}$ , and  $A_{\text{N}}$  (Table S4) have been determined, showing that within the experimental uncertainty the electronic distribution around Cu(II) ions is similar for all the studied compounds. When the molecular rotation is stopped upon freezing all the spectra become analogous. Arguably, the replacement of ligands carried out is mainly affecting the motional behavior of the complexes.

Finally, the X-band EPR spectrum of a frozen toluene solution of CuPcTB4 (Figure 4d) was simulated to determine the principal values of the  $g$ ,  $A_{\text{Cu}}$ , and  $A_{\text{N}}$  tensors. We fitted the spectrum by taking into consideration the presence of two resonant species, one containing  $^{63}\text{Cu}$  and the other  $^{65}\text{Cu}$ , both in their natural abundance (69.15 and 30.85 %, respectively). The derived parameters (Table S4), confirm the  $D_{4h}$  symmetry around the copper (II) ions in this compound as well as a considerable delocalization of the  $d$  electrons over the isoindole nitrogens.

As compared to the reference (CuPcTB4), the asymmetrical CuPcs has dissimilar electronic structure. However, it signals unique solid-state magnetic exchange, *i.e.* the packing of the molecules and thus the  $\pi$ - $\pi$  interactions and the energy of the frontier orbitals. These results are following the results of transient absorption, which suggests dissimilar substitutions show different lifetimes of excited state relaxation.

## 2.5 Photovoltaic performance of PSCs with ZnPcs as HTMs

To elucidate the significance of different substitutions and core metals on the performance of PSCs, we fabricated PSCs with the architect of FTO/*b&mp*-TiO<sub>2</sub>/perovskite/Pcs/Au (*b&mp*-TiO<sub>2</sub>: compact and mesoporous TiO<sub>2</sub> layers). The schematic of the PSCs and the cross-sectional SEM

image of the device with ZnPcAE as an HTM (Figure 1) display, well-defined layer-by-layer structure with sharp interfaces. The perovskite ( $\text{FA}_{1-y}\text{MA}_y\text{PbI}_{3-x}\text{Br}_x$ ) layer was prepared by a two-step deposition method ( $t = \sim 500$  nm), while ZnPcAE was spin-casted on the perovskite layer to serve as an HTM ( $t = \sim 112$  nm).

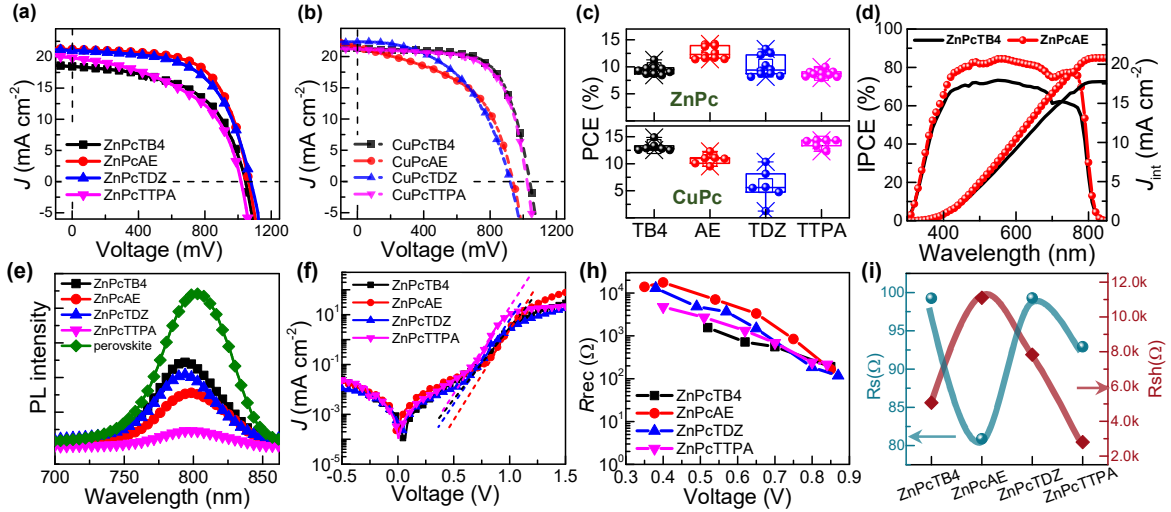


Figure 5.  $J$ - $V$  curves of the champion device with different (a) ZnPcs and (b) CuPcs as HTM and  $\text{b\&mp-TiO}_2$  as an ETM, (c) statistical efficiency performance of PSCs with ZnPc and CuPc HTMs. The average values were analyzed from ten devices for ZnPcs-based PSCs and six devices for CuPcs-based PSCs, respectively, (d) IPCE and integrated  $J_{\text{int}}$  of the device with ZnPcTB4, ZnPcAE as HTMs, (e) steady-state photoluminescence spectra of bare perovskite and perovskite with different ZnPc HTMs, (f)  $J$ - $V$  curves in the dark (the dash-dot lines present the fitting lines for  $J_0$  and  $n$ ). (g) the recombination resistance extracted from the impedance spectra plots for the device with different ZnPcs under different photovoltage. (h)  $R_s$  and  $R_{\text{sh}}$  values extracted from champion  $J$ - $V$  curves of the device with different ZnPcs under reverse scan.

Firstly, chloroform and chlorobenzene were probed to investigate the effect of solvents on the charge transport performance of ZnPcAE. The film deposited by chloroform solvent shows better

PV performance than chlorobenzene (Figure S32), and to decipher this, we analyzed the microstructure systemically. The UV-vis absorption of ZnPcAE deposited in different solvents gave similar peak and absorption intensity. We examined the surface microstructure of perovskite coated with ZnPcAE derived from different solvents (Figure S33). The film deposited by chlorobenzene displays undissolved solids on the surface, which will promote recombination centers and reduce the charge extraction abilities. The root-mean-square roughness (RMS) of perovskite/ZnPcAE prepared by chlorobenzene with  $\sim 17.2$  nm is higher than that prepared by chloroform, signals uniformity and smoothness which in turn will allow building the sharper interface for efficient hole transportation.

Table 2 The champion photovoltaic parameters of the PSCs based on different MPes.

HTM	$V_{oc}$ (mV)	$J_{sc}$ (mA cm <sup>-2</sup> )	FF (%)	PCE (%)
ZnPcTB4	1042.6	18.46	54.7	10.52
ZnPcAE	1063.5	21.19	63.2	14.25
ZnPcTDZ	1076.3	21.02	58.8	13.30
ZnPcTTPA	1016.6	19.83	49.5	9.97
ZnPcAE <sup>a</sup>	974.3	24.35	65.8	15.61
CuPcTB4	1044.9	21.29	66.9	14.87
CuPcAE	915.7	22.66	59.2	12.29
CuPcTDZ	925.2	22.32	50.1	10.34
CuPcTTPA	1028.8	21.14	66.0	14.35

<sup>a</sup> PSC based on SnO<sub>2</sub> as ETM, the rest are with *b&mp*-TiO<sub>2</sub> as ETM.

The  $J$ - $V$  curves of the device using different HTMs are shown (Figure 5a&5b) and the corresponding photovoltaic parameters are listed (Table 2). For the device with ZnPc as HTMs,

the device employing ZnPcTB4 exhibits a PCE of only 10.52% with a  $V_{oc}$  of 1042.6 mV,  $J_{sc}$  of 18.46 mA cm<sup>-2</sup>, and FF of 54.7%. Interestingly, after substitutions with other groups, all compounds show better device performance. Especially, the ZnPcAE HTM exhibit the highest PCE with 14.25% with a  $V_{oc}$  of 1063.5 mV,  $J_{sc}$  of 21.19 mA cm<sup>-2</sup>, and FF of 63.2%, which mainly resulted from the enhanced  $J_{sc}$  and  $FF$ . The average of PCE from the device with different HTMs show the similar trend (Figure 5c and Table S5). The  $J_{sc}$  values match with integrated current densities (20.8 mA cm<sup>-2</sup>) obtained from the incident photon-to-current conversion efficiency (IPCE) (Figure 5d), were indicating that ZnPcAE exhibits higher photon to electron conversion efficiency than ZnPcTB4 for the whole visible wavelength region. The  $V_{oc}$  of ZnPcTDZ presents the highest values than other ZnPcs, originated from the well-matched energy level. For the Zn-based Pcs, ZnPcAE (1.94 nm) and ZnPcTDZ (1.28 nm) owned the higher  $L_D$  than ZnPcTB4 (0.80 nm), and ZnPcTTPA (1.12 nm), and thus yield higher efficiency than ZnPcTB4/ZnPcTTPA.

We optimize the device performance of ZnPc based PSCs by replacing *mp*-TiO<sub>2</sub> with planar SnO<sub>2</sub> quantum dot as an ETM, reaching a PCE of 15.61% with  $V_{oc}$  of 974.2 mV,  $J_{sc}$  of 24.35 mA cm<sup>-2</sup>, and FF of 65.79% (Figure S34). We attribute this to SnO<sub>2</sub> unique properties such as higher conductivity and optical transparency compared to *mp*-TiO<sub>2</sub>. We investigated the hysteresis index ( $HI$ ) in champion devices by measuring  $J$ - $V$  curves under the forward and reverse scan directions. The device with ZnPcAE and ZnPcTDZ have quite small  $HI$  with 0.09 and 0.07, respectively (Figure S35 and Table S6).

On the other hand, considering the results of the PV device with ZnPcs, the device with CuPc analogs as HTMs should have a similar trend as of ZnPcs, however, they are dissimilar to the ZnPcs. The device with CuPcTB4 and CuPcTTPA yields higher efficiency than that of CuPcAE, CuPcTTPA. The device with CuPcTB4, CuPcTTPA exhibits the highest PCE of 14.87%, 14.35%,

higher than CuPcAE and CuPcTDZ with 12.29% and 10.34%, respectively. We noted difficulties to deposit uniform films for CuPcAE and CuPcTDZ. Although solvent engineering including chloroform/methanol mixed solvents for CuPcAE, chlorobenzene/tetrahydrofuran mixed solvent for CuPcTDZ, the corresponding efficiency is lower. The device with CuPcs (CuPcTB4, CuPcTTPA) shows higher efficiency than that of the device with Zn-based counterparts. The CuPcs owned a higher efficiency than the Zn-based counterparts, which can result in the higher charge transporting ability originated from their long lifetime. Considering the solubility issues with CuPcs, the discrepancy in device performance is difficult to correlate with their transportability. We investigated the carrier transportation difference employing ZnPc HTMs.

Steady-state photoluminescence (PL) measurement for perovskite using different ZnPcs with the film structure of quartz/perovskite/ZnPc was used to analyze the charge carrier transport process (Figure 5e). An emission peak centered at 803 nm for the pristine perovskite was observed. A reduced PL intensity was recognized for all the ZnPcs, indicating efficient hole carrier extraction from perovskite. Remarkably, a blue-shifted PL peak was observed for all the perovskite/ZnPcs, which can be ascribed to a decrease in the bulk and/or surface trap states in the perovskite layer after the deposition of thin layer of HTM.<sup>49</sup> ZnPcAE and ZnPcTDZ showed a large blue shift compared to other one, consequently, they showed lesser charge recombination at the interface between the perovskite and HTM layers measured by EIS and dark  $J$ - $V$  measurements indicating low value of reverse saturation current as discussed in below section. Subsequently, we noted improved PCE, due to enhancement in open circuit voltage ( $V_{oc}$ ) and short-circuit current.

To evaluate the function of different ZnPc HTMs on the performance of the PSCs dark current was measured (Figure 5f), the linear parts of the dark  $J$ - $V$  curves were fitted with the Shockley diode equation:  $J_D = J_0[\exp(qV/nK_B T)-1]$ , where  $J_0$  is the reverse saturation current density,  $J_D$  is

the dark current density,  $V$  is the applied bias,  $q$  is the electron charge,  $K_B$  is the Boltzmann constant,  $T$  is the temperature,  $n$  is the ideal factor of the real diode.<sup>50,51</sup> For devices with different ZnPc as HTMs,  $n$ , and  $J_0$  are listed in Table S7. The values of  $[n, J_0]$  was  $[2.94, 5.5 \times 10^{-6} \text{ mA cm}^{-2}]$ ,  $[2.3, 1.4 \times 10^{-7} \text{ mA cm}^{-2}]$ ,  $[2.6, 2.2 \times 10^{-6} \text{ mA cm}^{-2}]$ , and  $[2.4, 2.4 \times 10^{-6} \text{ mA cm}^{-2}]$  for the PSCs based on ZnPcTB4, ZnPcAE, ZnPcTDZ, ZnPcTTPA, respectively. The smaller value of  $n$  and  $J_0$  indicates a decrease in charge recombination at the interface between the perovskite and HTM layers. Thus, it is revealed that ZnPcAE reduces interface recombination and improves the transfer efficiency of the charge in the device, and leads to the high  $FF$  of the corresponding device.

To elucidate the charge transport kinetics (surface recombination, charge carrier diffusion, *etc.*) in devices based on developed ZnPcs, electrical impedance spectroscopy (EIS) was measured under different light intensities (0 – 0.2 Sun) of white LED illumination to produce different photovoltages.<sup>52</sup> An equivalent circuit was proposed ( $R$ - $R_{\text{rec}}$ / $C$ , Figure S37) to interpret the interface recombination.  $R$  is seen as the series resistance of the external circuit including connecting wires and two electrodes, and  $R_{\text{rec}}$  reflects the impact of recombination resistance of the device. In the typical Nyquist diagram of different devices with varying photovoltages (Figure S38), only  $R_{\text{rec}}$  values under a series of photovoltages from different ZnPc-based devices were extracted and plotted (Figure 5h) for discussion. With the increase in photovoltages, the value of  $R_{\text{rec}}$  decreases, due to the improvement in carrier concentration. At a similar potential bias, the  $R_{\text{rec}}$  values of the ZnPcAE-based device are beyond the values from other devices, which implies that ZnPcAE steeply reduced charge recombination at the perovskite/HTM interface.

The series resistance ( $R_s$ ) and shunt resistance ( $R_{\text{sh}}$ ) of devices was derived by fitting the  $J$ - $V$  curves measured in the reverse scan (Figure 5i). The ZnPcAE-based PSCs showed the lowest  $R_s$  of 81  $\Omega$ , whereas ZnPcTB4, ZnPcTDZ, ZnPcTTPA based- PSCs displayed the  $R_s$  of 99  $\Omega$ , 99  $\Omega$ ,

and 92  $\Omega$ , respectively. Moreover, the ZnPcAE-based device owned the highest  $R_{sh}$  of 11.1 k $\Omega$ , whereas ZnPcTB4, ZnPcTDZ, ZnPcTTPA based-device showed the  $R_{sh}$  of 5.1 k $\Omega$ , 7.8 k $\Omega$ , and 2.8 k $\Omega$ , respectively. The abilities to transport charge effectively are decisive for their performance of PSCs and the electrical conductivity for HTMs (Figure S36) was measured. The trend of  $R_{sh}$  is in agreement with the  $R_{rec}$ . The conductivity value in our condition follows the order: ZnPcAE ( $0.22 \mu\text{S cm}^{-1}$ ) > ZnPcTDZ ( $0.19 \mu\text{S cm}^{-1}$ ) > ZnPcTTPA ( $0.15 \mu\text{S cm}^{-1}$ ) > ZnPcTB4 ( $0.08 \mu\text{S cm}^{-1}$ ). Overall, the lowest  $R_s$  and highest  $R_{sh}$  of the ZnPcAE-based device yielded improved PCE with higher FF, which is ascribed to the relatively higher conductivity.

## 2.6 Device Stability performance

In addition to PSC performance, reliability is the crucial aspect to evaluate the performance of HTMs. To evaluate the surface nature, goniometer experiments were made to evaluate the hydrophobicity of perovskite films coated by different ZnPcs. The contact angles showed 99°, 97°, 99°, and 98°, respectively after spin-coating ZnPcTB4, ZnPcAE, ZnPcTDZ, and ZnPcTTPA atop of perovskite (Figure 6a), while that of perovskite with doped Spiro-OMeTAD is 75°. The perovskite coated ZnPcs samples yielded a contact angle over 90° and perovskite/ZnPcAE gave the highest value among them. The hydrophobic properties induced by ZnPcs can effectively prevent water from diffusing into the perovskite layer, thus leading to enhanced moisture stability. The substituted groups in asymmetrical ZnPcs also influence the surface properties marginally.



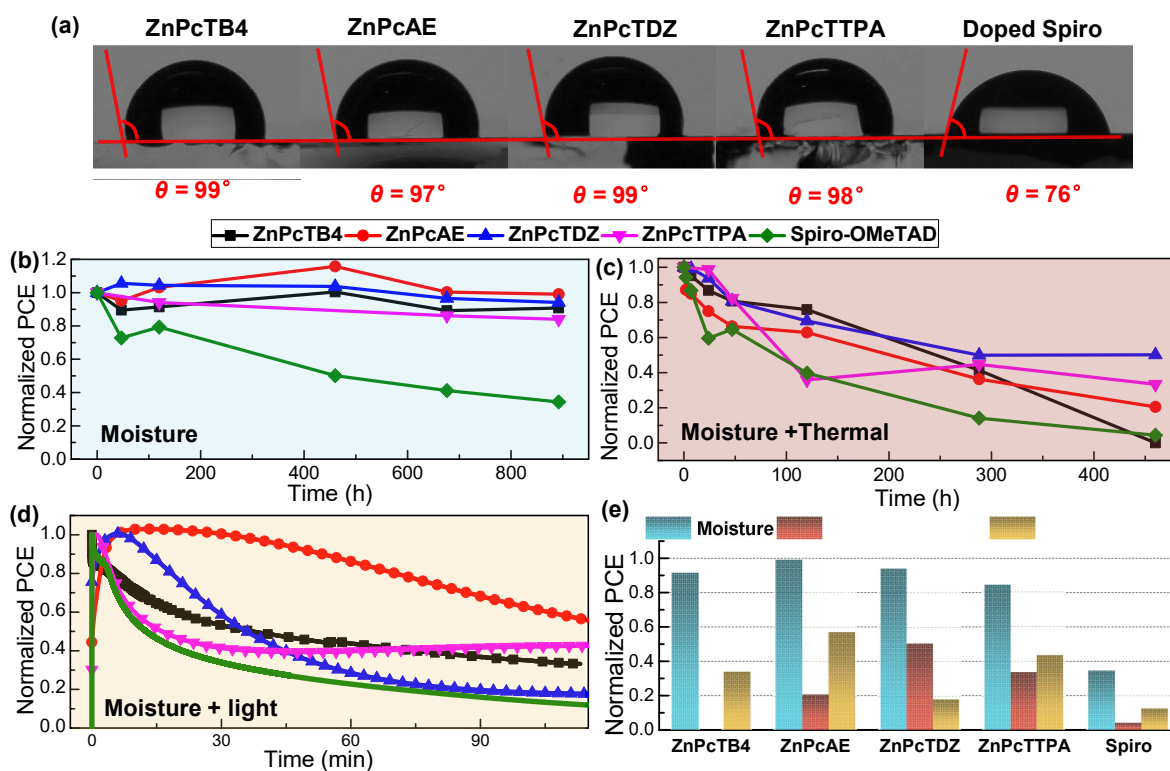


Figure 6. (a) Contact angles of perovskite with different ZnPcs and Spiro-OMeTAD, (b) PCE plots of PSCs with different ZnPcs and Spiro-OMeTAD aged under ambient condition (30-70% RH) for around 900 h, (c) plots of efficiency of PSCs based on different ZnPc and Spiro-OMeTAD HTMs under moisture and heat conditions, (d) maximum power point tracking under humidity and 1-sun illumination of the unencapsulated device with different HTMs and (e) normalized PCE obtained after aging condition. (Spiro: Spiro-OMeTAD).

For reliability purposes, the PSCs should operate under combined stress conditions instead of only one factor. To evaluate the potential of ZnPcs based PSCs, we investigated the stability of PSCs with ZnPcs under various stress conditions. Firstly, we measured the unencapsulated PSCs under the ambient condition with 30-70% relative humidity (RH), around 900 h (Figure 6b). The PCE based on ZnPcTB4, ZnPcAE, ZnPcTDZ, and ZnPcTTPA can retain 91%, 99%, 94%, and

84% of their initial PCE after aging, respectively, while the control device employing doped Spiro-OMeTAD as a HTM yielded around 17% (Figure S39) lost 70% of its initial PCE. The detailed PV parameters contain  $V_{oc}$ ,  $J_{sc}$ , and FF are shown (Figure S40). The  $J_{sc}$  values of ZnPc based PSCs remain unchanged, suggesting the perovskite can maintain the role as an active layer, but the  $J_{sc}$  value of the control device decrease to 50% of its initial value. UV-vis absorption spectra to study the degradation process of perovskite with different HTMs, was recorded at 550 nm wavelength vs time (Figure S41a). The perovskite with ZnPcs retains 80% absorbance of its initial values, while perovskite/Spiro-OMeTAD holds only 60% of the initial value. The visual image of perovskite layers with different HTMs after aging around 900 h was documented (Figure S41b). The perovskite/Spiro-OMeTAD displayed brown color instead of intense dark color, suggesting degradation of phase change. However, perovskite with ZnPcs showed dark color, indicating the entirety of perovskite with ZnPcs, which is consistent with the PV performance.  $FF$  value is related to the series resistance and ZnPcs-based PSCs retain >95% of their initial values after aging, suggesting ZnPcs create the rational interface between ZnPcs and perovskite. While the  $R_s$  value threefolds in the case of the control device (Figure S41c) suggesting, both the intrinsic poor stability of doped Spiro-OMeTAD and the decomposition of perovskite-induced dopant (lithium salt and *t*-BP) in Spiro-OMeTAD deteriorate the perovskite/HTM interface and the active layer.

Secondly, the devices were exposed to both environmental stress conditions (heat and humidity). The PV performance of PSCs was recorded under continuous thermal stress (85 °C) and ambient condition with 30-70% RH for around 500 h (Figure 6c), The PCE held 20%, 50%, and 33% of the initial value in the case of a device with ZnPcAE, ZnPcTDZ, ZnPcTTPA, respectively, but nearly 0% of the initial value was noted for ZnPcTB4, Spiro-OMeTAD-based PSCs. We noted that ZnPcAE, ZnPcTDZ, ZnPcTTPA showed competitive performance when exposed to heat and

high humidity conditions. The rate of the change of  $J_{sc}$  and  $FF$  for ZnPcAE, ZnPcTDZ, ZnPcTTPA-based PSCs was lower than that of ZnPcTB4 and control device (Figure S42). The change in  $R_s$  calculated by fitting the  $J-V$  curves as a function of time (Figure S41d), for ZnPcAE, ZnPcTDZ, ZnPcTTPA-based PSCs displayed increases to 3.0, 1.5, and 2.6 times of its initial values, respectively, while the control device expands to 24 times of initial value, which has a negative influence on device performance, especially  $J_{sc}$  and  $FF$  values. The Spiro-OMeTAD doped with lithium salt and *t*-BP undergoes morphological deformation at relatively high-temperature and produced large voids.<sup>53</sup> Besides, the photo-oxidation induced in an oxygen-rich environment and the crystallization and the aggregate formation of Spiro-OMeTAD deteriorate its transporting properties.<sup>54</sup> The poor performance of ZnPcTB4 under heat stress originates from an anchoring group that does not interact with the perovskite layer judiciously, as the presence of tert-*t*-butyl with other phthalocyanines can passivate the perovskite.

Further, we conducted maximum power point tracking of the unencapsulated devices under moisture (30-70% RH) with constant 1 sun illumination offered by white LED at room temperature (Figure 6d). The control device drastically drops to 11% of its initial value after 118 min. However, the device with ZnPcTB4, ZnPcAE, ZnPcTDZ, ZnPcTTPA maintained 33.4%, 56.8%, 17.7%, and 43.1% of their initial PCE, respectively. ZnPcs, especially ZnPcAE own excellent stability under humidity and light. The performance of the PSCs with different HTM under stress conditions (Figure 6e), suggests dopant-free ZnPcAE yielded improved stability as compared to ZnPc and traditional Spiro-OMeTAD.

### 3. Conclusion

We designed and quantify the physicochemical properties of a series of asymmetrically MPcs based on MPcTB4 (M = Zn or Cu) with AE, TDZ, and TTPA substituents and their influence on

electro-optical and photovoltaic properties. The charge carrier dynamics of MPcs suggest a comparable average lifetime in ZnPc for varied substitutions, while CuPcs own a longer lifetime than Zn-based analog. However, the ZnPcs signals a substantial difference in the amplitude, which can lead to an ample singlet character in the  $T_1$  state. This, in turn, impact the charge transport parameters such as mobility, the diffusion length of ZnPcAE, which are higher than similar ZnPcs. which is favorable for charge carrier extraction and transport in perovskite-based devices. The fabricated perovskite solar cells with ZnPcAE as hole selective layer gave a competitive photovoltaic performance in its pristine form. Notably, the devices showed significant stability under multi-stress conditions.

#### ASSOCIATED CONTENT

#### **SUPPORTING INFORMATION:**

The materials, and detailed synthesis and corresponding characterization such as FT-IR, NMR, HR-MALDI-TOF, Cyclic voltammetry for all novel developed materials; Additional experimental details for device fabrication and characterizations; Experimental details for transient absorbance absorption and electron paramagnetic resonance; GIXRD patterns of ZnPc on different substrates, morphology analysis for perovskite/ZnPc films; experimental and simulated X-band EPR; Solvent optimization for ZnPcAE HTM; device performance for ZnPcAE and ZnPcTDZ, and Spiro-OMeTAD HTM; Nyquist curves for device with different ZnPc HTMs. Additional stability performance under different conditions; Additional table for CV, and fitting parameters for ZnPc's curves, Spin Hamiltonian parameters and average PV parameters.

## Corresponding Author

E-mail: [shahzada.ahmad@bcmaterials.net](mailto:shahzada.ahmad@bcmaterials.net); [asastre@umh.es](mailto:asastre@umh.es)

## Author Contributions

† These authors contributed equally.

## Notes:

The authors declare no competing financial interest.

## ACKNOWLEDGMENTS

This work received funding from the European Union H2020 Programme under a European Research Council Consolidator grant [MOLEMAT, 726360]. We gratefully acknowledge the financial support provided by European Regional Development Fund “A way to make Europe and the Spanish Ministerio de Ciencia e Innovacion, Agencia Estatal de Investigación: project CTQ2017-87102-R AEI/FEDER, UE. P. H. acknowledges funding from the European Commission via a Marie-Skłodowska-Curie individual fellowship (SMILIES, No. 896211).

## REFERENCES

- (1) NREL Best Research-Cell Efficiencies. <https://www.nrel.gov/pv/cell-efficiency.html> (accessed in March, 2021).
- (2) Liu, Z.; Li, J.; Yan, F. Package-Free Flexible Organic Solar Cells with Graphene Top Electrodes. *Adv. Mater.* **2013**, *25* (31), 4296–4301. <https://doi.org/10.1002/adma.201205337>.
- (3) Kojima, A.; Teshima, K.; Shirai, Y.; Miyasaka, T. Organometal Halide Perovskites as

- Visible-Light Sensitizers for Photovoltaic Cells. *J. Am. Chem. Soc.* **2009**, *131* (17), 6050–6051. <https://doi.org/10.1021/ja809598r>.
- (4) Ponseca, C. S.; Savenije, T. J.; Abdellah, M.; Zheng, K.; Yartsev, A.; Pascher, T.; Harlang, T.; Chabera, P.; Pullerits, T.; Stepanov, A.; Wolf, J.-P.; Sundström, V. Organometal Halide Perovskite Solar Cell Materials Rationalized: Ultrafast Charge Generation, High and Microsecond-Long Balanced Mobilities, and Slow Recombination. *J. Am. Chem. Soc.* **2014**, *136* (14), 5189–5192. <https://doi.org/10.1021/ja412583t>.
  - (5) Stranks, S. D.; Eperon, G. E.; Grancini, G.; Menelaou, C.; Alcocer, M. J. P.; Leijtens, T.; Herz, L. M.; Petrozza, A.; Snaith, H. J. Electron-Hole Diffusion Lengths Exceeding 1 Micrometer in an Organometal Trihalide Perovskite Absorber. *Science* (80-. ). **2013**, *342* (6156), 341–344. <https://doi.org/10.1126/science.1243982>.
  - (6) Salado, M.; Andresini, M.; Huang, P.; Khan, M. T.; Ciriaco, F.; Kazim, S.; Ahmad, S. Interface Engineering by Thiazolium Iodide Passivation Towards Reduced Thermal Diffusion and Performance Improvement in Perovskite Solar Cells. *Adv. Funct. Mater.* **2020**, *30* (14), 1910561. <https://doi.org/10.1002/adfm.201910561>.
  - (7) Huang, P.; Yuan, L.; Zhang, K.; Chen, Q.; Zhou, Y.; Song, B.; Li, Y. Room-Temperature and Aqueous Solution-Processed Two-Dimensional TiS<sub>2</sub> as an Electron Transport Layer for Highly Efficient and Stable Planar n-i-p Perovskite Solar Cells. *ACS Appl. Mater. Interfaces* **2018**, *10* (17), 14796–14802. <https://doi.org/10.1021/acsami.8b03225>.
  - (8) Huang, P.; Wang, Z.; Liu, Y.; Zhang, K.; Yuan, L.; Zhou, Y.; Song, B.; Li, Y. Water-Soluble 2D Transition Metal Dichalcogenides as the Hole-Transport Layer for Highly Efficient and Stable p-i-n Perovskite Solar Cells. *ACS Appl. Mater. Interfaces* **2017**, *9* (30), 25323–25331. <https://doi.org/10.1021/acsami.7b06403>.
  - (9) Huang, P.; Chen, Q.; Zhang, K.; Yuan, L.; Zhou, Y.; Song, B.; Li, Y. 21.7% Efficiency Achieved in Planar n-i-p Perovskite Solar Cells via Interface Engineering with Water-Soluble 2D TiS<sub>2</sub>. *J. Mater. Chem. A* **2019**, *7* (11), 6213–6219. <https://doi.org/10.1039/c8ta11841h>.
  - (10) Urbani, M.; de la Torre, G.; Nazeeruddin, M. K.; Torres, T. Phthalocyanines and Porphyrinoid Analogues as Hole- and Electron-Transporting Materials for Perovskite Solar Cells. *Chem. Soc. Rev.* **2019**, *48* (10), 2738–2766. <https://doi.org/10.1039/C9CS00059C>.
  - (11) Calió, L.; Kazim, S.; Grätzel, M.; Ahmad, S. Hole-Transport Materials for Perovskite Solar

- Cells. *Angew. Chemie Int. Ed.* **2016**, *55* (47), 14522–14545. <https://doi.org/10.1002/anie.201601757>.
- (12) Caliò, L.; Salado, M.; Kazim, S.; Ahmad, S. A Generic Route of Hydrophobic Doping in Hole Transporting Material to Increase Longevity of Perovskite Solar Cells. *Joule* **2018**, *2* (9), 1800–1815. <https://doi.org/10.1016/j.joule.2018.06.012>.
- (13) Ren, G.; Han, W.; Deng, Y.; Wu, W.; Li, Z.; Guo, J.; Bao, H.; Liu, C.; Guo, W. Strategies of Modifying Spiro-OMeTAD Materials for Perovskite Solar Cells: A Review. *J. Mater. Chem. A* **2021**, *9* (8), 4589–4625. <https://doi.org/10.1039/D0TA11564A>.
- (14) Yin, X.; Song, Z.; Li, Z.; Tang, W. Toward Ideal Hole Transport Materials: A Review on Recent Progress in Dopant-Free Hole Transport Materials for Fabricating Efficient and Stable Perovskite Solar Cells. *Energy Environ. Sci.* **2020**, *13* (11), 4057–4086. <https://doi.org/10.1039/D0EE02337J>.
- (15) Kim, S. W.; Kim, G.; Moon, C. su; Yang, T. Y.; Seo, J. Metal-Free Phthalocyanine as a Hole Transporting Material and a Surface Passivator for Efficient and Stable Perovskite Solar Cells. *Small Methods* **2021**, *5* (5). <https://doi.org/10.1002/smt.202001248>.
- (16) Yu, Z.; Wang, L.; Mu, X.; Chen, C.; Wu, Y.; Cao, J.; Tang, Y. Intramolecular Electric Field Construction in Metal Phthalocyanine as Dopant-Free Hole Transporting Material for Stable Perovskite Solar Cells with >21 % Efficiency. *Angew. Chemie Int. Ed.* **2021**, *60* (12), 6294–6299. <https://doi.org/10.1002/anie.202016087>.
- (17) Cheng, M.; Li, Y.; Safdari, M.; Chen, C.; Liu, P.; Kloo, L.; Sun, L. Efficient Perovskite Solar Cells Based on a Solution Processable Nickel(II) Phthalocyanine and Vanadium Oxide Integrated Hole Transport Layer. *Adv. Energy Mater.* **2017**, *7* (14), 1602556. <https://doi.org/10.1002/aenm.201602556>.
- (18) Molina, D.; Ruiz-Preciado, M. A.; Carlsen, B.; Eickemeyer, F. T.; Yang, B.; Flores-Díaz, N.; Álvaro-Martins, M. J.; Nonomura, K.; Hagfeldt, A.; Sastre-Santos, Á. Zinc Phthalocyanine Conjugated Dimers as Efficient Dopant-Free Hole Transporting Materials in Perovskite Solar Cells. *ChemPhotoChem* **2020**, *4* (4), 307–314. <https://doi.org/10.1002/cptc.201900245>.
- (19) Hu, Q.; Rezaee, E.; Li, M.; Chen, Q.; Cao, Y.; Mayukh, M.; McGrath, D. V.; Xu, Z.-X. Molecular Design Strategy in Developing Titanyl Phthalocyanines as Dopant-Free Hole-Transporting Materials for Perovskite Solar Cells: Peripheral or Nonperipheral

- Substituents? *ACS Appl. Mater. Interfaces* **2019**, *11* (40), 36535–36543. <https://doi.org/10.1021/acsami.9b09490>.
- (20) Huang, P.; Hernández, A.; Kazim, S.; Ortiz, J.; Sastre-Santos, Á.; Ahmad, S. Molecularly Engineered Thienyl-Triphenylamine Substituted Zinc Phthalocyanine as Dopant Free Hole Transporting Materials in Perovskite Solar Cells. *Sustain. Energy Fuels* **2020**, *4* (12), 6188–6195. <https://doi.org/10.1039/D0SE01215G>.
- (21) Fukuzumi, S.; Ohkubo, K.; Ortiz, J.; Gutiérrez, A. M.; Fernández-Lázaro, F.; Sastre-Santos, Á. Formation of a Long-Lived Charge-Separated State of a Zinc Phthalocyanine-Perylenediimide Dyad by Complexation with Magnesium Ion. *Chem. Commun.* **2005**, No. 30, 3814. <https://doi.org/10.1039/b506412k>.
- (22) Blas-Ferrando, V. M.; Ortiz, J.; Follana-Berná, J.; Fernández-Lázaro, F.; Campos, A.; Mastorrent, M.; Sastre-Santos, Á. Large-Size Star-Shaped Conjugated (Fused) Triphthalocyaninehexaazatriphenylene. *Org. Lett.* **2016**, *18* (6), 1466–1469. <https://doi.org/10.1021/acs.orglett.6b00412>.
- (23) Fukuzumi, S.; Ohkubo, K.; Ortiz, J.; Gutiérrez, A. M.; Fernández-Lázaro, F.; Sastre-Santos, Á. Control of Photoinduced Electron Transfer in Zinc Phthalocyanine-Perylenediimide Dyad and Triad by the Magnesium Ion. *J. Phys. Chem. A* **2008**, *112* (43), 10744–10752. <https://doi.org/10.1021/jp805464e>.
- (24) Leznoff, C. C.; Svirskaya, P. I.; Khouw, B.; Cerny, R. L.; Seymour, P.; Lever, A. B. P. Syntheses of Monometalated and Unsymmetrically Substituted Binuclear Phthalocyanines and a Pentanuclear Phthalocyanine by Solution and Polymer Support Methods. *J. Org. Chem.* **1991**, *56* (1), 82–90. <https://doi.org/10.1021/jo00001a019>.
- (25) Liao, M.-S.; Scheiner, S. Electronic Structure and Bonding in Metal Phthalocyanines, Metal=Fe, Co, Ni, Cu, Zn, Mg. *J. Chem. Phys.* **2001**, *114* (22), 9780–9791. <https://doi.org/10.1063/1.1367374>.
- (26) Bhattacharya, S.; Reddy, G.; Paul, S.; Hossain, S. S.; Kumar Raavi, S. S.; Giribabu, L.; Samanta, A.; Soma, V. R. Comparative Photophysical and Femtosecond Third-Order Nonlinear Optical Properties of Novel Imidazole Substituted Metal Phthalocyanines. *Dye. Pigment.* **2021**, *184* (July 2020), 108791. <https://doi.org/10.1016/j.dyepig.2020.108791>.
- (27) Doria, S.; Lapini, A.; Di Donato, M.; Righini, R.; Azzaroli, N.; Iagatti, A.; Caram, J. R.; Sinclair, T. S.; Cupellini, L.; Jurinovich, S.; Mennucci, B.; Zanotti, G.; Paoletti, A. M.;



- Pennesi, G.; Foggi, P. Understanding the Influence of Disorder on the Exciton Dynamics and Energy Transfer in Zn-Phthalocyanine H-Aggregates. *Phys. Chem. Chem. Phys.* **2018**, *20* (34), 22331–22341. <https://doi.org/10.1039/c8cp02172d>.
- (28) Feng, Y.; Hu, Q.; Rezaee, E.; Li, M.; Xu, Z. X.; Lorenzoni, A.; Mercuri, F.; Muccini, M. High-Performance and Stable Perovskite Solar Cells Based on Dopant-Free Arylamine-Substituted Copper(II) Phthalocyanine Hole-Transporting Materials. *Adv. Energy Mater.* **2019**, *9* (26), 1901019. <https://doi.org/10.1002/aenm.201901019>.
- (29) Ling, X.; Wu, J.; Xu, W.; Zhang, J. Probing the Effect of Molecular Orientation on the Intensity of Chemical Enhancement Using Graphene-Enhanced Raman Spectroscopy. *Small* **2012**, *8* (9), 1365–1372. <https://doi.org/10.1002/sml.201102223>.
- (30) Hu, L.; Wang, W.; Liu, H.; Peng, J.; Cao, H.; Shao, G.; Xia, Z.; Ma, W.; Tang, J. PbS Colloidal Quantum Dots as an Effective Hole Transporter for Planar Heterojunction Perovskite Solar Cells. *J. Mater. Chem. A* **2015**, *3* (2), 515–518. <https://doi.org/10.1039/C4TA04272G>.
- (31) Zheng, X.; Wang, Y.; Hu, J.; Yang, G.; Guo, Z.; Xia, J.; Xu, Z.; Fang, G. Octamethyl-Substituted Pd(  $\text{C}_{10}\text{H}_{16}\text{N}_4$  ) Phthalocyanine with Long Carrier Lifetime as a Dopant-Free Hole Selective Material for Performance Enhancement of Perovskite Solar Cells. *J. Mater. Chem. A* **2017**, *5* (46), 24416–24424. <https://doi.org/10.1039/C7TA07216C>.
- (32) Iagatti, A.; Doria, S.; Marcelli, A.; Angelini, N.; Notarantonio, S.; Paoletti, A. M.; Pennesi, G.; Rossi, G.; Zanotti, G.; Calogero, G.; Foggi, P. Photophysical Processes Occurring in a Zn-Phthalocyanine in Ethanol Solution and on TiO<sub>2</sub> Nanostructures. *J. Phys. Chem. C* **2015**, *119* (35), 20256–20264. <https://doi.org/10.1021/acs.jpcc.5b04978>.
- (33) Kakade, S.; Ghosh, R.; Palit, D. K. Excited State Dynamics of Zinc-Phthalocyanine Nanoaggregates in Strong Hydrogen Bonding Solvents. *J. Phys. Chem. C* **2012**, *116* (28), 15155–15166. <https://doi.org/10.1021/jp304369r>.
- (34) Peumans, P.; Yakimov, A.; Forrest, S. R. Small Molecular Weight Organic Thin-Film Photodetectors and Solar Cells. *J. Appl. Phys.* **2003**, *93* (7), 3693–3723. <https://doi.org/10.1063/1.1534621>.
- (35) Abramczyk, H.; Brozek-Płuska, B.; Kurczewski, K.; Kurczewska, M.; Szymczyk, I.; Krzyczmonik, P.; Błaszczak, T.; Scholl, H.; Czajkowski, W. Femtosecond Transient Absorption, Raman, and Electrochemistry Studies of Tetrasulfonated Copper

- Phthalocyanine in Water Solutions. *J. Phys. Chem. A* **2006**, *110* (28), 8627–8636. <https://doi.org/10.1021/jp060322a>.
- (36) Caplins, B. W.; Mullenbach, T. K.; Holmes, R. J.; Blank, D. A. Femtosecond to Nanosecond Excited State Dynamics of Vapor Deposited Copper Phthalocyanine Thin Films. *Phys. Chem. Chem. Phys.* **2016**, *18* (16), 11454–11459. <https://doi.org/10.1039/c6cp00958a>.
- (37) Nikolaitchik, A. V. Crown Ether Substituted Monomeric and Cofacial Dimeric Metallophthalocyanines. 1. Photophysical Studies of the Free Base, Zinc(II), and Copper(II) Variants. *J. Phys. Chem. A* **1999**, *103* (38), 7587–7596. <https://doi.org/10.1021/jp9911651>.
- (38) Ha-Thi, M.-H.; Shafizadeh, N.; Poisson, L.; Soep, B. An Efficient Indirect Mechanism for the Ultrafast Intersystem Crossing in Copper Porphyrins. *J. Phys. Chem. A* **2013**, *117* (34), 8111–8118. <https://doi.org/10.1021/jp4008015>.
- (39) Kumar, P. H.; Venkatesh, Y.; Siva, D.; Ramakrishna, B.; Bangal, P. R. Ultrafast Relaxation Dynamics of 5,10,15,20- Meso- Tetrakis Pentafluorophenyl Porphyrin Studied by Fluorescence up-Conversion and Transient Absorption Spectroscopy. *J. Phys. Chem. A* **2015**, *119* (8), 1267–1278. <https://doi.org/10.1021/jp512137a>.
- (40) Bhattacharya, S.; Biswas, C.; Raavi, S. S. K.; Venkata Suman Krishna, J.; Koteswar, D.; Giribabu, L.; Venugopal Rao, S. Optoelectronic, Femtosecond Nonlinear Optical Properties and Excited State Dynamics of a Triphenyl Imidazole Induced Phthalocyanine Derivative. *RSC Adv.* **2019**, *9* (63), 36726–36741. <https://doi.org/10.1039/C9RA07758H>.
- (41) Kroeze, J. E.; Savenije, T. J.; Candeias, L. P.; Warman, J. M.; Siebbeles, L. D. A. Triplet Exciton Diffusion and Delayed Interfacial Charge Separation in a TiO<sub>2</sub>/PdTPPC Bilayer: Monte Carlo Simulations. *Sol. Energy Mater. Sol. Cells* **2005**, *85* (2), 189–203. <https://doi.org/10.1016/j.solmat.2004.04.015>.
- (42) Abkowitz, M.; Chen, I.; Sharp, J. H. Electron Spin Resonance of the Organic Semiconductor,  $\alpha$ -Copper Phthalocyanine. *J. Chem. Phys.* **1968**, *48* (10), 4561–4567. <https://doi.org/10.1063/1.1668028>.
- (43) Guzy, C. M.; Raynor, J. B.; Symons, M. C. R. Electron Spin Resonance Spectrum of Copper-63 Phthalocyanine. A Reassessment of the Bonding Parameters. *J. Chem. Soc. A Inorganic, Phys. Theor.* **1969**, 2299. <https://doi.org/10.1039/j19690002299>.
- (44) Finazzo, C.; Calle, C.; Stoll, S.; Van Doorslaer, S.; Schweiger, A. Matrix Effects on Copper(II)Phthalocyanine Complexes. A Combined Continuous Wave and Pulse EPR and

- DFT Study. *Phys. Chem. Chem. Phys.* **2006**, *8* (16), 1942. <https://doi.org/10.1039/b516184c>.
- (45) Moons, H.; Łapok, Ł.; Loas, A.; Van Doorslaer, S.; Gorun, S. M. Synthesis, X-Ray Structure, Magnetic Resonance, and DFT Analysis of a Soluble Copper(II) Phthalocyanine Lacking C–H Bonds †. *Inorg. Chem.* **2010**, *49* (19), 8779–8789. <https://doi.org/10.1021/ic100814j>.
- (46) Greiner, S. P.; Rowlands, D. L.; Kreilick, R. W. EPR and ENDOR Study of Selected Porphyrin- and Phthalocyanine-Copper Complexes. *J. Phys. Chem.* **1992**, *96* (23), 9132–9139. <https://doi.org/10.1021/j100202a012>.
- (47) Hathaway, B. J.; Billing, D. E. The Electronic Properties and Stereochemistry of Mono-Nuclear Complexes of the Copper(II) Ion. *Coord. Chem. Rev.* **1970**, *5* (2), 143–207. [https://doi.org/10.1016/S0010-8545\(00\)80135-6](https://doi.org/10.1016/S0010-8545(00)80135-6).
- (48) Hudson, A.; Luckhurst, G. R. Electron Resonance Line Shapes of Radicals in Solution. *Chem. Rev.* **1969**, *69* (2), 191–225. <https://doi.org/10.1021/cr60258a003>.
- (49) de Quilettes, D. W.; Vorpahl, S. M.; Stranks, S. D.; Nagaoka, H.; Eperon, G. E.; Ziffer, M. E.; Snaith, H. J.; Ginger, D. S. Impact of Microstructure on Local Carrier Lifetime in Perovskite Solar Cells. *Science* (80-. ). **2015**, *348* (6235), 683–686. <https://doi.org/10.1126/science.aaa5333>.
- (50) Kyaw, A. K. K.; Wang, D. H.; Gupta, V.; Leong, W. L.; Ke, L.; Bazan, G. C.; Heeger, A. J. Intensity Dependence of Current–Voltage Characteristics and Recombination in High-Efficiency Solution-Processed Small-Molecule Solar Cells. *ACS Nano* **2013**, *7* (5), 4569–4577. <https://doi.org/10.1021/nn401267s>.
- (51) Shi, J.; Dong, J.; Lv, S.; Xu, Y.; Zhu, L.; Xiao, J.; Xu, X.; Wu, H.; Li, D.; Luo, Y.; Meng, Q. Hole-Conductor-Free Perovskite Organic Lead Iodide Heterojunction Thin-Film Solar Cells: High Efficiency and Junction Property. *Appl. Phys. Lett.* **2014**, *104* (6), 063901. <https://doi.org/10.1063/1.4864638>.
- (52) Huang, P.; Manju; Kazim, S.; Sivakumar, G.; Salado, M.; Misra, R.; Ahmad, S. Pyridine Bridging Diphenylamine-Carbazole with Linking Topology as Rational Hole Transporter for Perovskite Solar Cells Fabrication. *ACS Appl. Mater. Interfaces* **2020**, *12* (20), 22881–22890. <https://doi.org/10.1021/acsami.0c03584>.
- (53) Jena, A. K.; Ikegami, M.; Miyasaka, T. Severe Morphological Deformation of Spiro-

- OMeTAD in (CH<sub>3</sub>NH<sub>3</sub>)PbI<sub>3</sub> Solar Cells at High Temperature. *ACS Energy Lett.* **2017**, *2* (8), 1760–1761. <https://doi.org/10.1021/acsenergylett.7b00582>.
- (54) Sanchez, R. S.; Mas-Marza, E. Light-Induced Effects on Spiro-OMeTAD Films and Hybrid Lead Halide Perovskite Solar Cells. *Sol. Energy Mater. Sol. Cells* **2016**, *158*, 189–194. <https://doi.org/10.1016/j.solmat.2016.03.024>.